Biosensors and Bioelectronics 132 (2019) 162–170

Contents lists available at ScienceDirect

Biosensors and Bioelectronics

journal homepage: www.elsevier.com/locate/bios

Nanoplasmonic swarm biosensing using single nanoparticle colorimetry

Mengxing Ouyang, Dino Di Carlo*

Department of Bioengineering, University of California, Los Angeles, CA 90095, USA

ARTICLE INFO

Keywords:
Nanoplasmonic biosensor
Single nanoparticle
Protein marker detection
Point-of-care

ABSTRACT

We demonstrate a swarm biosensing platform that detects analyte based on the change in plasmonic signal from thousands of single nanoparticles sensors, leading to increased quantitative accuracy. Following dark field microscopy, we perform computational image registration and analyses to compile the hue change from thousands of single gold nanoparticles acting as individual quantitative biosensors. This platform demonstrated a limit of detection of 10 pM with a dynamic range of at least 4 orders of magnitude in buffer solution, and the successful detection of c-reactive protein (CRP) in serum compatible with 3-tier clinical cutoffs within a 10-fold difference without the need for a blocking step. By analyzing the before-and-after status of each plasmonic sensor, our sensing scheme provides informative sensing capabilities with the flexibility to select a subset of nanoparticles with optimal performance based on their initial states. Hue comparisons within and among devices also render the platform tolerant to particle and device variation. In addition, the simplicity of the readout instrumentation based on optical imaging and the implementation of microfluidics make it promising for future adaptation into point-of-care systems.

1. Introduction

Nanoplasmonic sensors (Anker et al., 2008; Brolo, 2012) have become a promising solution for sensing of bio-analytes. Due to strong light localization, these nanosensors are sensitive to even a few molecules that when bound to their surface perturb the electromagnetic field distribution. Indeed, detection sensitivity down to a single molecule level has been demonstrated (Ament et al., 2012; Zijlstra et al., 2012). Despite the significant progress in the development of nanoplasmonic biosensors, few of these approaches have yet to reach commercial products for point-of-care diagnostics. The main hurdles are associated with achieving both compact instrumentation and robust sensing performance for practical use (Csaki et al., 2018; Hill, 2015; Lopez et al., 2017; Spackova et al., 2016; Vashist et al., 2015). In general, biosensing measurements are affected by variability in surface properties in different devices, the imperfections in manufacture of sensing elements, biological noise such as non-specific binding, and measurement noise introduced by the readout system, which together lead to systematic and random errors. For biosensing applications from clinical samples, the sensor performance is further negatively affected by the matrix effect (Chiu et al., 2010; Johnsson et al., 2002; Situ et al., 2008) in biofluids, causing reduced target binding and elevated background noise.

Conventional nanoplasmonic detection schemes typically measure the collective signal from an ensemble of nanosensors which yields an averaged sensor readout as a single measurement, where the properties of individual particles remain unseen within an integrated spectrum (Sonntag et al., 2014). Many recent nanoplasmonic sensors have been reported using ensemble signals for biomarker detection in biofluids, such as spectral shift (Im et al., 2014; Inci et al., 2015), intensity (Chen et al., 2015), and area ratio with maximum brightness (Liang et al., 2017). An ensemble measurement not only loses information from individual nanosensors and compromises the detection sensitivity, but also introduces random noise due to the lack of repeated measurements on the same sample. In bulk measurements, particle size variation may broaden the spectral signature and reduce detection resolution, which cannot be efficiently improved even when averaged spectral shifts is used as an output. On the other hand, measuring signal shifts of single nanoparticles allows the examination of particle variation and the minimization of systematic error at single particle resolution, which cannot be achieved using bulk measurements. Sensing with single nanoparticles providing individual readouts has been explored (Ament et al., 2012; Chen et al., 2011; Mayer et al., 2010; McFarland and Van Duyne, 2003; Raschke et al., 2003), but spectral imaging on a large number of particles requires bulky and expensive setups for hyperspectral imaging, otherwise only low throughput ($n \leq 120$) (Hao et al., 2014; Hill, 2015) has been achieved with manual interrogation. All these factors hinder the adoption of nanoplasmonic sensors for point-of-

* Corresponding author.
E-mail address: dicarlo@ucla.edu (D. Di Carlo).

https://doi.org/10.1016/j.bios.2019.02.056
Received 3 October 2018; Received in revised form 12 January 2019; Accepted 18 February 2019
Available online 04 March 2019
0956-5663/

care applications.

Individual nanoplasmonic sensors can also have variable readouts. Since the nanoplasmonic effect is a near-field phenomenon, only binding events that occur at tens of nanometers around the sensor surface will affect the sensor signal. Therefore, the matrix effect and bulk background noise is greatly suppressed. However, these nanosensors (with critical dimensions from 40 to 100 nm) have limited binding sites on their surface (typically 100–1000 binding sites). As a result, when the analyte concentration is much lower than the affinity of the capture antibody being used, the dynamic binding process leads only to a small fraction of bound analyte-antibody states. For example, at low analyte concentration of ~10 pM, only ~1/10–1/100 of surface antibodies are converted to bound states based on the Langmuir adsorption model, assuming a typical affinity for antibody-antigen pairs of 100 pM – 1 nM (Landry et al., 2015). Therefore, an individual nanosensor only captures on the order of 10 molecules. In addition, plasmonic nanosensors have highly inhomogeneous optical field distributions. Therefore, the sensor signal strongly depends on the location where the analyte is bound on the sensor surface with respect to the direction of optical excitation. These, taken together, introduce a large statistical uncertainly in optical signal among individual nanosensors.

As a critical step towards the development of a portable nanoplasmonic biosensor, we demonstrate a swarm biosensing platform based on a low-cost dark field imaging setup, where the color signal from each single nanoparticle sensor was collected and analyzed. The readout of these individual "votes", i.e., color shifts, from multiple sensors were then compiled to determine a reliable sensing result that normalizes for systematic error and obtains higher statistical accuracy of representing the dynamic binding process. Specifically, the device is composed of a multitude of single gold nanoparticles (AuNPs) dispersed on an optically transparent surface which can be individually interrogated. Instead of measuring spectral shift averaged from many colloidal nanoparticles, or an assembly of nanostructures on a surface, we use a CMOS color camera to image the hue change of individual nanoparticles by extracting the RGB information for each nanoparticle from dark field images. A few hundreds to over a thousand single nanoparticles were identified within one imaging field of view (172 μm × 122 μm), leading to thousands of single nanoparticles per sample, enabling statistical analysis of sensing outputs from a large number of sensors for each device. Detector AuNPs were used to amplify the color shift, which has proven to yield 3 to 7-fold enhanced spectral shift in conventional spectrum-based detection (Hall et al., 2011; Nguyen and Sim, 2015; Spadavecchia et al., 2013). This amplification allows us to achieve a similar level of sensitivity (~pM) without the need of recovering the spectrum information, thus keeping the setup compact and low-cost. In addition, our swarm sensing platform exhibited a large dynamic range (> 4 orders of magnitude), and high quantitation ability to reliably differentiate three clinically relevant CRP concentrations (in a narrow range of 1–10 μg/ml) in human serum. Compared with conventional approaches that rely on averaged signal from a localized ensemble of particles without correlation at the single-particle level, our swarm sensing approach recognizes individual signal shifts from a large population of single particles, and therefore achieves more consistent sensor readouts despite particle or device variations. These key features will allow future adaptation to nanoplasmonic point-of care assays, where robust quantitative readout in a small form factor is critical for use in rapid turnaround time tests in clinical or community health settings.

2. Materials and methods

2.1. Conjugation of gold nanoparticles

Spherical gold nanoparticles (Nanopartz™, A11-citrate-capped) was centrifuged and resuspended in 1 mM 11-mercaptoundecanoic acid (MUA, 450561, Sigma-Aldrich) for reaction overnight. N-(3-Dimethylaminopropyl)-N′-ethylcarbodiimide hydrochloride (EDC, E6383, Sigma-Aldrich) and n-hydroxysuccinimide (NHS, 130672, Sigma-Aldrich) solution was mixed in MES buffer at 1:2 ratio. AuNPs in MUA solution was centrifuged and resuspended in EDC/NHS (0.1/0.2 mM) in 10 mM MES buffer and reacted for 30 min. The AuNP solution was then centrifuged and resuspended in antigen or antibody solution followed by 2 h incubation at room temperature. For Anti-BSA detection, 2 μM BSA (Sigma) was used for both capture and detector AuNPs. For CRP detection, 0.1 mg/ml Anti-CRP antibody C5 (ab8279, Abcam) and C6 (ab8278, Abcam) were used for 100 nm and 10 nm AuNPs, respectively. The final nanoparticle-conjugates were centrifuged and resuspended in DI water for later use.

2.2. Spectra measurements

A UV–Vis spectrophotometer (GENESYS™ 10S, Thermo Fisher) was used to monitor the spectral shift of AuNPs in colloidal solutions during conjugation. For each measurement, 500 μL of solution was added to the cuvette and measured against blank, i.e., DI water. For direct binding confirmation, a series of anti-BSA (200 μM) solutions were added to the cuvette containing 500 μL of AuNP solution sequentially at 2 min intervals, followed by an immediate spectral measurement after each addition. The volume of anti-BSA added was 1 μL over 5 times, and lastly 5 μL for the binding to reach saturation. The resulting solution was then centrifuged and resuspended in DI water to remove unbound molecules and obtain the final measurement.

2.3. Imaging setup and image analysis

The dark field imaging setup is composed of a 60x dark field objective (NA 0.7), dark field condenser (NA 0.85–0.95), and a color camera (DS-Fi3) mounted to an inverted microscope, all purchased from Nikon. First, an initial image of the immobilized capture nanoparticles in the liquid solution was taken, namely the "before" image. Then, the target analyte was added to the sensor surface and incubated at room temperature followed by a washing step. Next, detector AuNPs was added to the sensor surface for another incubation. Excess and unbound detector AuNPs were washed away, and images of the same locations were taken as "after" images. Both the "before" and "after" images were taken with cover slip correction when AuNPs were immersed in liquid solution. Typically, imaging acquisition for both timepoints could be completed within 5 min in total. Region of interests (ROIs) were defined in the "before" images to identify each single particle sensor with the hue value of each sensor converted from RGB readout. Spectral overlapping among neighboring AuNPs were eliminated automatically from the data pool by imaging analysis algorithm with the use of parameters such as circularity and area. ImageJ was used to align the "before" and "after" color images from the same field of view (Thevenaz et al., 1998), define ROIs of the individual AuNPs based on a threshold of brightness, and extract the mean R, G, B value from each ROI to calculate the hue value before and after sensing. Parameters such as circularity and area were used to select ROIs representing single particles. Finally, delta hue was determined by subtracting the after-hue value from before-hue value.

2.4. SEM of AuNPs

Bare and conjugated AuNP colloidal solutions were dispersed on a silicon substrate, dried and imaged using scanning electron microscopy (Supra 40VP SEM, ZEISS) at 10 kV.

2.5. Finite-difference time-domain (FDTD) simulation

FDTD software from Lumerical Inc. was used to numerically simulate the 3D scattering spectrum of a gold nanoparticle. The total-field scatter-field (TFSF) source was used to simulate dark field imaging. A

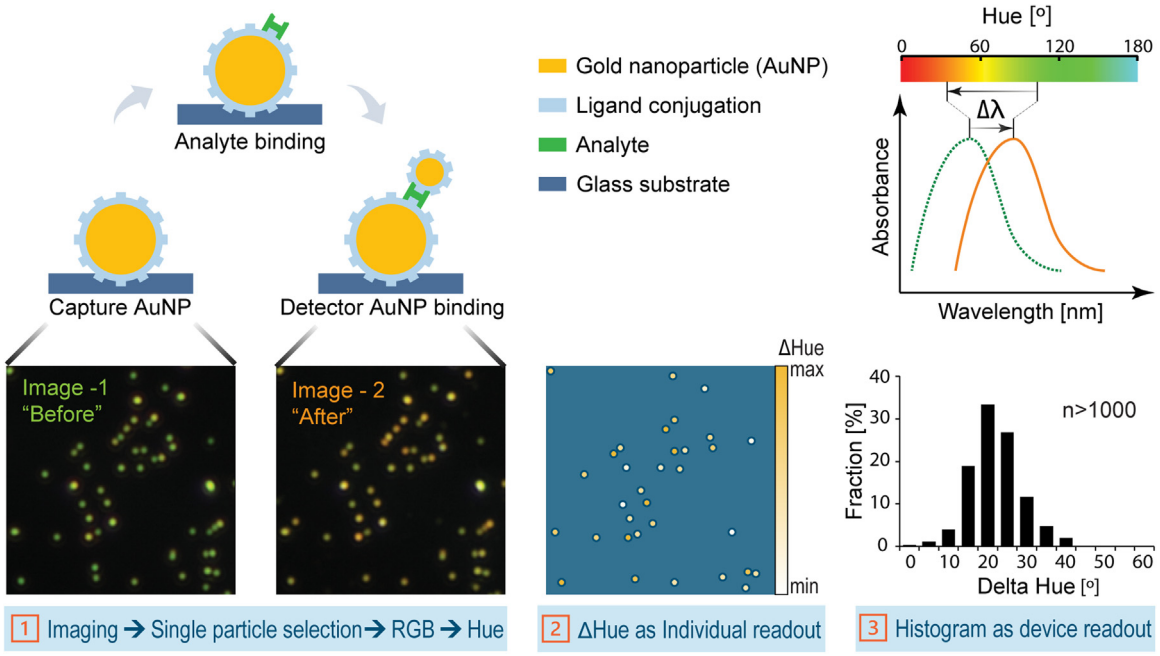

Fig. 1. Schematic of the nanoplasmonic sensing platform using a swarm of single nanoparticle colorimetric sensors. The spectral shifts due to the binding of sandwiched AuNP pairs correlates with a detectable hue shift of the individual nanoparticles using a color camera. Analyte detection is performed as follows: Capture AuNPs conjugated with analyte-specific ligand are first immobilized and a "before" image is taken to record each individual sensor's initial hue; Then, target analyte and detector AuNPs were added sequentially, incubated on chip, and washed; Finally, the "after" sensing image was taken at the same location to record the final resulting hue. The delta hue of each individual nanoparticle was compiled to generate a histogram representing the sensor readout.

100 nm-AuNP was placed inside the TFSF. The background index was set as 1.3 (for water). A frequency-domain power monitor was placed outside of the TFSF source to collect the scattered signal. In our experimental setup, the numerical aperture (NA) of the objective was 0.7. Therefore, the size of the power monitor (square shaped) was set twice the distance of the monitor from the AuNP, which resulted in a collection half-angle of 45°. A shell thicknesses of 2.5, 5, 7.5 nm, respectively, with refractive index of 1.45 were placed surrounding the AuNP to simulate the functionalized antibody layer. The electromagnetic field decay length of the 100 nm AuNP was estimated to be 20 nm. To simulate the binding of 10 nm-AuNPs (with shell layer 2.5, 5 and 7.5 nm), we generated random positions on the surface of the 100 nm-AuNP with the criteria that the positions generated for each consecutive 10 nm-AuNP has to be non-overlapping with any existing 10 nm-AuNP. Otherwise, a new random position was generated, until no new random positions were available to satisfy the non-overlapping condition within 1000 trials. The resonance spectrum obtained from FDTD simulation was converted to RGB values by overlapping with the color-matching functions defined by the International Commission on Illumination (CIE). Then, the RGB values were converted to the hue value.

2.6. Nanoplasmonic on-chip detection in water

Capture AuNPs with 100 nm diameters and detector AuNPs with 10 nm diameters were both conjugated with BSA in a colloidal solution. A glass coverslip was treated with poly-L-lysine (P8920, Sigma-Aldrich) for 10 min and washed three times with DI water and dried. Then, capture AuNPs were immobilized on the glass coverslip. To immobilize, the solution containing capture AuNP-BSA conjugates was added to a microchannel bound to the glass coverslip and incubated for 2 h followed by washing 3 times to remove excess unbound AuNPs. The before images of immobilized capture AuNPs were first taken at different locations on the coverslip in DI water. Then, the solution in the microchannel was replaced with anti-BSA (B7276, Sigma-Aldrich) solution and incubated for 15 min at room temperature. This solution was then washed once with DI water and the BSA-conjugated detector AuNP solution was added. After a 30 min incubation, the chip was washed 3 times with DI water and a second set of images at previously recorded fields of view were taken, which are defined as "after" images. The exposure time used for imaging was 120 ms.

2.7. CRP detection in water and serum

Capture AuNPs with 100 nm diameters and detector AuNPs with 10 nm diameters were conjugated with anti-CRP C5 and C6 (Sigma-Aldrich) in a colloidal solution, respectively. For initial CRP detection tests, DI water was used as a dilution solvent. For detection in serum, CRP (236603, Sigma-Aldrich) was spiked into CRP free serum (Hytest, Netherland) to constitute CRP in serum at concentrations of 1, 3, and 10 μg/ml, respectively. Similar to the detection of anti-BSA in water, the before images of immobilized capture AuNPs were first taken at different locations on the coverslip. Then, solution was replaced with CRP spiked serum and incubated for 15 min. Then, the chip was washed once with DI water and detector AuNPs were added. After a 30 min incubation, the chip was washed 3 times with DI water and the "after" images were taken. For CRP detection in serum in which we included a blocking step to compare, a commercial blocking buffer (37584, Thermo Fisher) was used. The exposure time used for imaging was 120 and 150 ms for detection in DI water and serum, respectively.

3. Results

3.1. Chip design and detection scheme

AuNPs with diameters of 100 nm were immobilized in a microchannel sandwiched between two glass coverslips. Antibodies were functionalized on gold nanoparticles in the colloidal phase before the immobilization step using conventional EDC/NHS methods (detailed in Methods). Surface treatment using poly-L-lysine promoted adhesion of nanoparticles to the substrate and ensured robust attachment withstanding washing steps. We used the UV–Vis spectrum shift to verify the above surface functionalization process (Fig. S1). To validate the

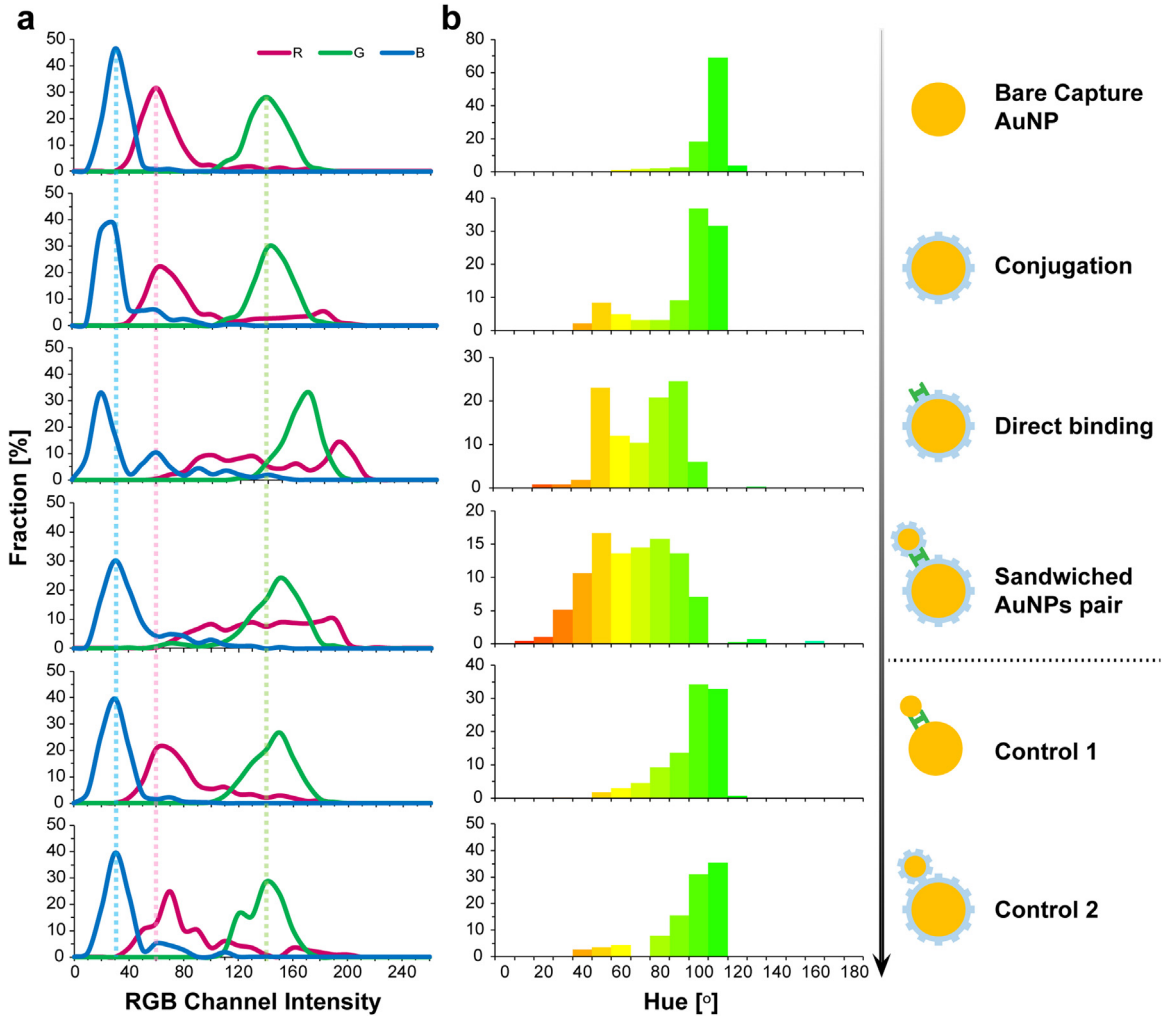

Fig. 2. Study of **(a)** RGB shifts and **(b)** hue shifts due to conjugation, direct binding and detector AuNP binding in a colloidal state. AuNP solutions after each step were added onto a glass coverslip, dried, and then imaged in darkfield. Histograms of hue for individual particles show significant changes in hue are visible.

binding of the chosen antigen and antibody pairs, we further monitored the UV–Vis spectrum shift after adding different concentrations of antigens into the antibody functionalized-AuNP colloid solution (Fig. S2). To minimize the instrument complexity, our swarm biosensing protocol was based on comparing two dark field images on the nanoparticles immobilized on the sensor chip, free from spectroscopic measurement (Fig. 1). An initial image of the immobilized nanoparticles before addition of analyte (i.e., "before" image) was taken using a CMOS color-camera. Next, the sample solution was injected into the microchannel between two cover slips, followed by the injection of detector AuNPs of much smaller size (typically ~10 nm) that were functionalized with a paired antibody to amplify the protein binding signal on the capture AuNP. Last, a second dark field image was taken at the same field of view as the "after" image" (detailed in Methods). A sample image of quantitation for each particle after image analysis is shown in Fig. S3. A histogram of the delta hue from all the single nanoparticle sensors was compiled to obtain the representative detection results of one chip (Fig. 1). Total assay time is less than one hour, which includes 10–15 min of target analyte incubation, and 30 min detector probe incubation, imaging acquisition and washing steps.

3.2. Selection of AuNP pairs

The optimal sizes of the paired capture and detector AuNPs were selected to maximize the hue shifts caused by binding events. Ideal capture AuNPs would maintain sufficient scattered light intensity to provide a high detection baseline, while detector AuNPs preferred would exhibit minimal background signal interference without binding. AuNPs with diameters of 20, 60, 100 and 150 nm were evaluated as capture probes under the same imaging conditions, where 100 nm and 150 nm particles appeared green and orange, respectively, with high intensity (Table S1). In addition, the color camera operates at higher quantum efficiency at wavelengths around 550 nm (i.e. correlating with green hue), implying greater signal to noise ratio at this region. Therefore, AuNPs with 100 nm diameter were selected as capture probes. For the detector particles, AuNPs with diameters of 4, 10, 20 and 60 nm were evaluated based on several criteria (Table S2). The ideal candidate would be easy to conjugate, yield a low background signal during dark field imaging, and enhance the hue shift when sandwiched with the capture AuNPs. Therefore, smaller AuNPs (< 10 nm) were not desirable due to technical difficulty during conjugation as they require ultra-high centrifugation speeds as well as their inability to enhance the hue signal when sandwiched to the capture nanoparticle. On the other hand, larger AuNPs (> 20 nm) adhered non-specifically and led to a larger background noise which may interfere with the signal from capture AuNPs. In the end, 10 nm AuNPs were chosen as detector probes because they were less prone to provide a false positive signal while providing a similar delta hue when compared to sandwiches formed using 20 nm AuNPs. Furthermore, FDTD simulations indicated that 100 nm capture AuNPs allow a maximum number

of ~ 100 detector AuNPs of 10 nm to bind, creating a hue change of up to 14 (Fig. S4). Therefore, each single AuNP functions as a quantitative biosensor with a large number of levels in the analog readout.

3.3. Delta hue for individual nanoparticle readout

RGB and HSV are alternative color models. During data analysis, RGB information acquired from raw images was converted to HSV in terms of hue, saturation, and value. Hue, which is independent of intensity and saturation, directly correlates with the dominant wavelength, and therefore has been used as an alternative approach to spectral measurement (Cheng et al., 2014; Hao et al., 2014; Jing et al., 2012). On the other hand, the other two elements of the HSV color space, i.e., saturation and value are susceptible to interference from imaging conditions, and failed to establish correlation with analyte concentrations (Fig. S5). Therefore, the signal to noise ratio was significantly enhanced by converting RGB to HSV and using only hue as the quantitative readout.

We monitored and analyzed the color change using RGB and hue of individual AuNPs in each consecutive step during the development of swarm sensors (Fig. 2). The 100 nm-AuNP-conjugates remained a green hue with a slight decrease (~10°) compared to unconjugated 100 nm AuNPs. A drastic shift of hue was demonstrated in the histograms of AuNP-conjugates bound with Anti-BSA as more single particles exhibited light green/yellow/light orange hues. This hue shift was further enhanced when the detector AuNPs were added, where the percentage of particles with yellow/orange/red increased; achieving ~40° hue shift for the population on average. Two control conditions were included and showed that neither non-specific binding of bare AuNP pairs randomly sandwiched with target analytes, nor the binding between capture and detector conjugates yielded significant hue shifts on average. The RGB information for each condition (Fig. 2**a**) provided insights into the cause of the hue shift. The drastic increase in the red channel value and moderate increase in the green channel value contributed to the hue shift from green to orange/red. The blue channel remained relatively constant throughout all groups, suggesting its potential use as a reference during image acquisition.

3.4. Swarm sensor characterization in buffer

We characterized the sensitivity and dynamic range of our system using two different proteins in buffer solution. The detection of anti-BSA concentrations ranging from 10 pM to 10 μM was demonstrated, which yielded a shift in the delta hue histogram comprising each sensor's individual readout (Fig. 3**a**). The large sample size of the sensor swarm ($n > 2000$ individual nanoparticle sensors for each device) better enabled differentiation ($p < 0.05$) between neighboring concentrations with a 10-fold concentration difference. The dynamic range using the mean value of the delta hue (Fig. 3**b**) was 6 orders of magnitude with a limit of detection of 10 pM. Detection of CRP in DI water from 1 ng/ml to 10 μg/ml revealed a dynamic range of at least 4 orders of magnitude with the potential to detect even lower concentrations (Fig. 3**c-d**). We chose 1 ng/ml (i.e., 8.7 pM) as the lower end of detection because it was comparable to the lowest anti-BSA concentration (i.e., 10 pM) tested. Since the clinical cutoffs are in the μg/ml range, the detection of CRP concentrations lower than 1 ng/ml was not pursued. The detection performance could be affected by the variation of protein markers, affinity of the antigen-antibody pair, as well as protein structure and dimension. The linear range was determined to be over 3 orders of magnitude for Anti-BSA (10 pM to 10 nM, $R^2 > 0.99$), and 4 orders of magnitude for CRP (1 ng/ml to 10 μg/ml, $R^2 > 0.99$).

3.5. Detection of a cardiac biomarker in serum

For practical applications, robust and accurate quantitation are essential features for biomarker detection in clinical settings. For example, CRP, a common inflammation marker, has been demonstrated to be valuable at lower concentrations, i.e., < 10 μg/ml, in both primary and secondary cardiovascular prophylaxis as a predictive marker to evaluate the risk of cardiac diseases. According to Centers for Disease Control and Prevention (CDC) guidelines, CRP levels lower than 1 μg/ml, within 1 and 3 μg/ml, and within 3 and 10 μg/ml are classified as low, intermediate and high coronary risks, respectively (Adukauskiene et al., 2016b; Pearson et al., 2003). The recommendation of this high-sensitivity CRP (hsCRP) assessment for patients with moderate risk of cardiovascular disease has been implemented in several countries in recent years, i.e., American Heart Association and CDC in United States in 2003, Canadian Cardiology Society in 2009, and European Society of Cardiology in 2012 (Adukauskiene et al., 2016a). We challenged our swarm sensing system with hsCRP detection in human serum at clinical cutoffs at 1, 3, and 10 μg/ml. The peak of the stacked histogram shifted to larger delta hue as CRP concentration increased (Fig. 4**a**); The mean delta hue from three devices was used to represent the detection output (Fig. 4**b**) with each of the clinical ranges found to be statistically distinct ($p < 0.05$), demonstrating the ability to successfully differentiate between the three clinical cutoffs with good sensor reproducibility. Furthermore, we have compared the results of CRP detection in serum with and without blocking at two clinically relevant concentrations (i.e., 1 and 10 μg/ml), and no significant difference was found (Fig. S6).

4. Discussion

4.1. Optimal swarm size

Our swarm sensing platform aims at robust and accurate quantification, where the random noise due to a variety of sources discussed previously can be minimized by compiling readout from a large number of single nanoparticles in the swarm (i.e. large swarm size). Statistically, a large sample size leads to a tighter confidence interval, indicating a greater precision in the final measurement output (Springate, 2012). This approach, however, may not always be practical due to increased instrumentation complexity and labor needed for repeated measurements. The swarm sensing scheme provides the flexibility to significantly increase sample size by imaging multiple single sensors as independent measurements without increasing instrumentation complexity or prolonging detection time. The standard error of hue shift decreases as the swarm size increases, which converged at around 2000 (Fig. S7). Therefore, a swarm size of 2000 single nanoparticles achieves the trade-off between high fidelity and measurement complexity, beyond which, the standard error, which indicates the accuracy of sample mean compared to the population mean, would not be significantly improved with increased swarm size. This optimal swarm size is expected to be similar across analytes of the same size. However, an optimization experiment is recommended if gold nanoparticles of significantly different sizes, or other LSPR materials are used.

4.2. Wide dynamic range using single nanoparticle swarms

As demonstrated in Section 3.2, AuNPs with 100 nm and 10 nm diameters achieve quantitative analog delta hue readout for individual AuNPs with random error minimized by assessing the majority “votes”. For nanoplasmonic sensing, the swarm sensor system provides significant advantages over “digital” assays, which evaluates individual sensing events with binary “on” and “off” output (Rissin et al., 2010), in terms of dynamic range, operational concentrations and sensing accuracy. Although a digital nanoplasmonic assay employing AuNP dimer structure (80 nm and 40 nm respectively) achieved a low limit of detection, it significantly limited the dynamic range of the assay (Ungureanu et al., 2010; Verdoold et al., 2011). With limited binding sites available on the surface of a single 80 nm-AuNP for 40 nm-AuNPs detector probes, only qualitative binary readout was achieved for

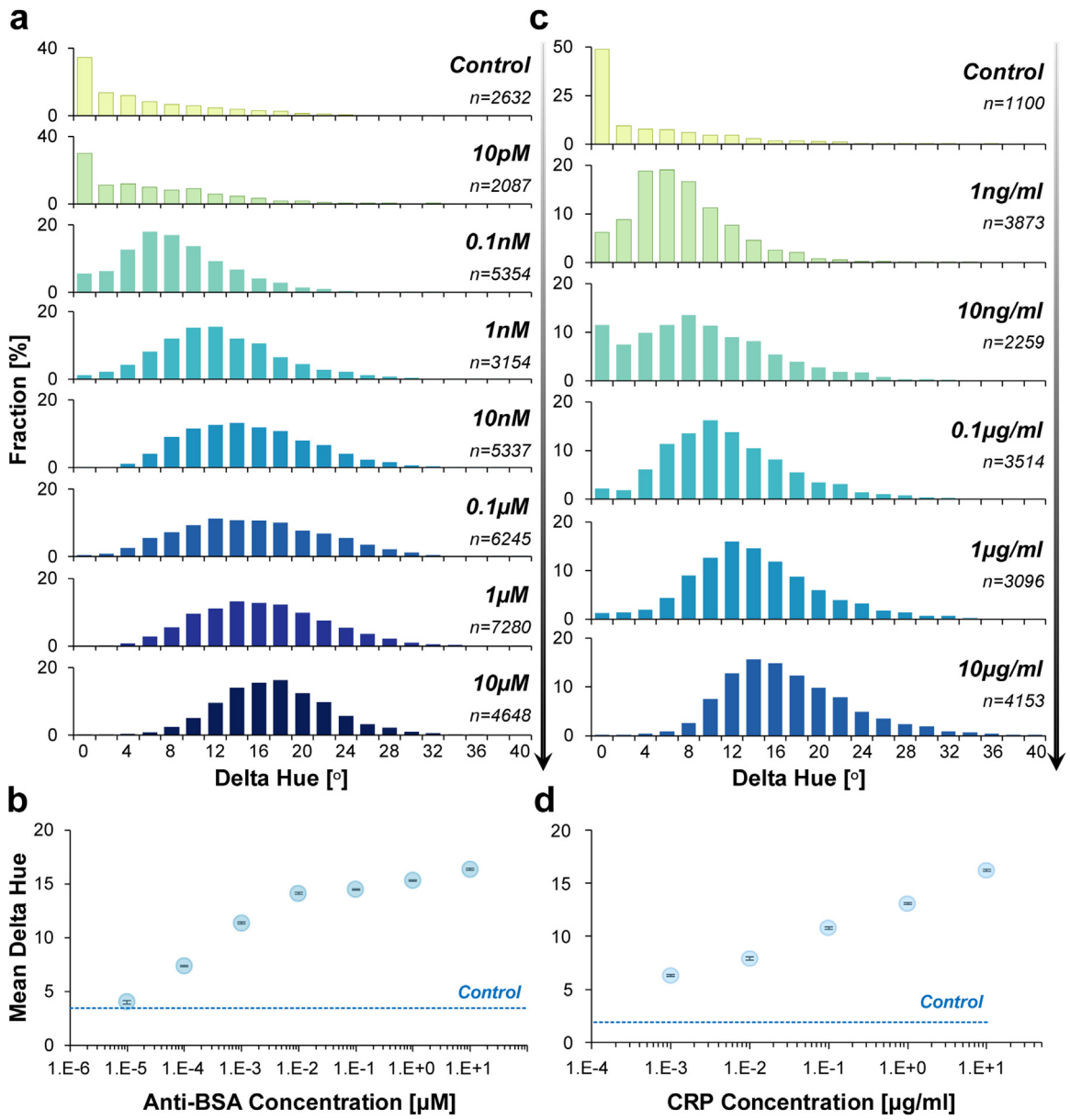

Fig. 3. System characterization using **(a-b)** anti-BSA and **(c-d)** CRP as the analyte in DI water. For each analyte, **(a,c)** the histogram of sensing output from a nanoparticle swarm and **(b,d)** mean value of delta hue for different concentrations of analyte are shown. In the control group, DI water was added instead of antibody solution, followed by detector AuNPs. The error bars in (b) and (d) represent standard error σ_n of each device, which is calculated by $\sigma_n = \sigma/\sqrt{n}$, where σ is the standard deviation of the population, and n is the sample size. For all groups, sample size $n > 1100$ single nanoparticles.

individual AuNPs, and collectively one quantitative readout was generated per device representing the fraction of AuNPs with a positive color change, i.e., R/G ratio. As a result, this system exhibited a narrow dynamic range (2 orders of magnitude) in buffer solution and approached saturation at ultra-low concentrations (sub-picomolar). Our swarm sensor overcomes this problem by utilizing a much smaller detector AuNP (10 nm) paired with a large capture AuNP (100 nm) and demonstrated that the hue change induced by the binding of 10 nm-AuNPs on a single 100-nm AuNP can be quantitatively characterized over a range of concentrations – achieving a quantitative analog signal per sensor particle. Experimental data indicated an average hue shift from 4° to 16° was observed for each individual capture nanoparticle bound with a noise level around 2–3° (Fig. 3**b, d**). This agrees well with FDTD simulation results that a maximum number of ~100 10 nm-AuNPs could bind to the surface of a single 100 nm-AuNP, inducing hue shifts ranging from 2° to 14° (Fig. S4). Analysis of the histogram of a swarm of thousands (≥ 2000) AuNPs further improved the detection resolution by reducing the uncertainty of the delta hue to ~0.1, as indicated by the standard error of the swarm (Fig. 3**b, d**). Therefore, a much wider dynamic range (4–6 logs) was achieved for protein detection using swarm sensing.

4.3. Improved sensing accuracy using individual hue shifts

A quantitative comparison was conducted to evaluate the uncertainty using an ensemble measurement of delta hue. i.e., mean of pre-hue – mean of after-hue, versus the distribution from individual hue shifts. The uncertainty of an ensemble measurement, represented by the standard deviation, is calculated based on error propagation, $\sigma_{ensemble} = \sqrt{\sigma_{pre-hue}{}^2 + \sigma_{after-hue}{}^2}$. The uncertainty of individual hue shifts is instead represented by its standard deviation, $\sigma_{individual}$. Analysis of CRP detection revealed that an ensemble measurement exhibited much greater uncertainty compared to individual hue shifts, i.e.,1.4–2.6 fold higher standard deviation compared to swarm sensing in buffer,

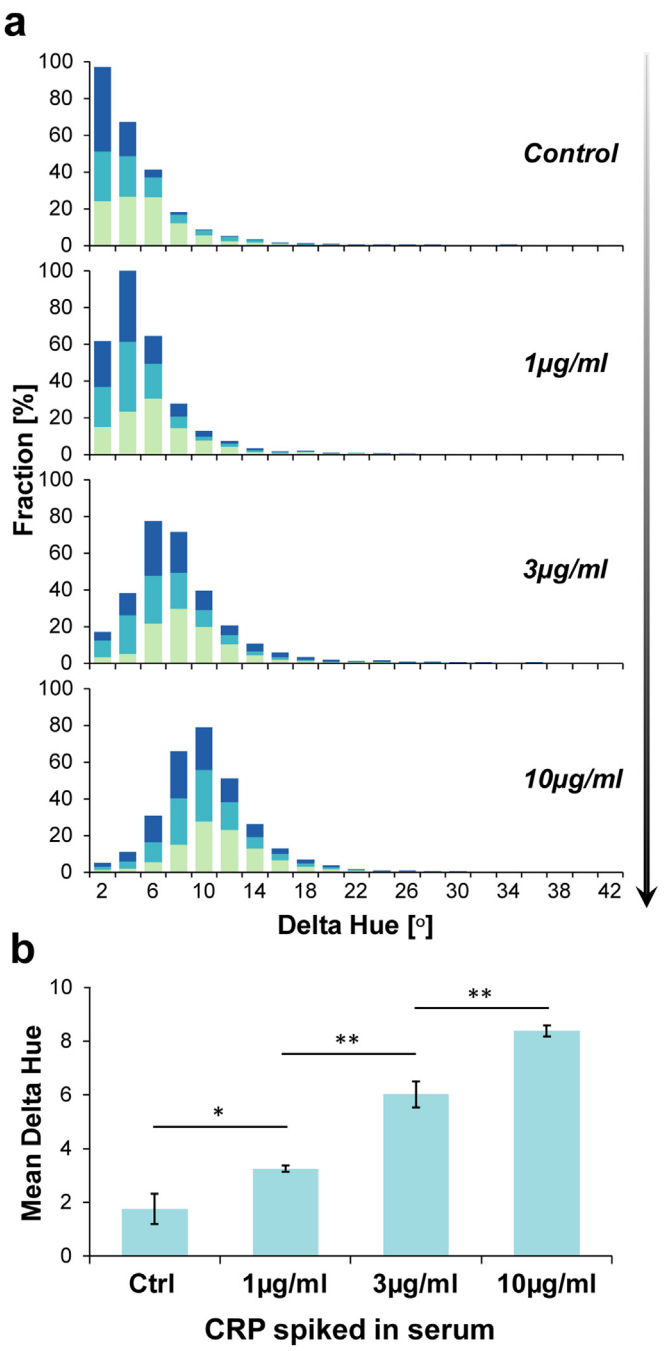

Fig. 4. Detection of CRP in human serum at clinically relevant concentrations. **(a)** The histogram and **(b)** mean value of delta hue is shown as a function of CRP concentration. Stacked histograms are pooled from three separate experiments, with each color representing a different experiment. The error bars in (b) represent the standard deviation of the mean value of the nanoparticle swarm from three devices. In the control group, CRP-free serum was added instead of CRP antibody solution, followed by detector AuNPs. *p*-values were determined by two-tailed student *t*-tests. $*p < 0.05$, $**p < 0.01$. For all groups, sample size $n > 2000$.

and 2.5–4.4 fold in serum, respectively. This suggests that using swarm sensing could improve detection accuracy in particular in a clinical setting. For an ideal device, where all the single particles possess identical initial states and are predicted to perform in the same manner, only one set of dark field images would be necessary, after all of the reaction steps. In reality, the hue of individual sensors in the same field of view varies slightly (as seen in the "before" image in Fig. 1), leading to systematic error that is unique for each sensor. Compared to the analytical results using delta hue (Figs. 3 and 4), results only using after-hue failed to establish a consistent trend with the increase of target analyte concentrations in buffer solutions (Fig. S8); and failed to differentiate among the three clinical ranges with statistical significance for detection in serum (Fig. S9), jeopardizing the confidence when interpreting sensor readouts. Many factors could contribute to the hue variations of single nanoparticle sensors before detection, such as size distribution due to the fabrication process of bare particles (e.g., the hue histogram of bare particles, as shown in Fig. 2**b**) and conjugation efficiencies (e.g., the before-hue histogram of capture AuNPs conjugated with BSA/Anti-CRP, as shown in Fig. 5). In addition, dark field images only illustrate the scattered light from nanoparticles, which is typically larger than the actual particle size, therefore, the region of a single ROI does not represent the exact shape of an individual nanoparticle. During image analysis, parameters such as circularity and area of the ROI have been used as filters to facilitate the selection of single particles, however it is still possible that a circular ROI was in fact an aggregate of multiple nanoparticles. Accurate detection readout could also be affected by either the particle variation caused by conjugation, or the inconsistency of initial states of sensor chips during immobilization or imaging conditions. Overall, swarm sensing based on delta hue led to readout that was more tolerable to both individual particle variations (Fig. 3), and device variation (Fig. 4).

4.4. High tolerance to non-specific binding for sensing in complex biofluids

Biosensing in biofluids remains challenging, as sensor performance is typically hindered by issues such as non-specific binding (Tokel et al., 2014) and sample variation, which is largely due to the complex nature and matrix effect of the biofluids. Furthermore, biomarker detection becomes even more difficult when the clinical cutoffs are within a close range (e.g., < 10-fold). For example, the clinically relevant concentrations of CRP as a cardiac marker are at relatively high concentrations (i.e., μg/ml) with only ~3 times concentration differences (Adukauskiene et al., 2016b; Pearson et al., 2003). Our approach using swarm sensing based on delta hue appears to be less sensitive to the non-specific binding on the device surface (Fig. S6), i.e., false positive signal was minimized. One potential reason is that since ROIs were predefined by the "before" image, only signals from the areas corresponding to nanoparticle sensors were analyzed. In addition, the detector probes (AuNPs with 10 nm diameter) do not generate interfering signal alone because the exposure time used during dark field imaging was too low for these smaller nanoparticles to generate sufficient scattered light alone. On the other hand, despite the interference of matrix effects exerted on the assay performance, i.e., lower signal (Fig. 5**b-c**), our parallel swarm detection scheme avoids sources of systematic and random errors introduced by sample matrices, and differentiates clinical cutoffs with < 10 fold difference in concentration with robust readouts, demonstrating significant potential for biosensing in clinical settings.

4.5. Informative sensing by examining pre-hue vs. delta-hue

Because the status of each single nanoparticle sensor before and after sensing were both recorded, we were able to map the detection results of each single nanoparticle versus its initial state, which provides further "quality control" capabilities to identify optimal/reliable sensors in the swarm. The scatter plot of each device with thousands of single particle sensors typically shows a triangular shape (Fig. S10). The distribution of before-hue on the x-axis represents the sensor variation due to particle size and conjugation using different protein markers, e.g., BSA and anti-CRP (Fig. 5**a-b**). As shown in the before-hue histogram in Fig. 5, the majority of the sensor population initially exhibited a hue around 80°. We hypothesize that the region in between 70° to 90° represents typical 100 nm diameter single nanoparticles with a complete conjugation layer. Higher before-hue (> 90°), which is very rare,

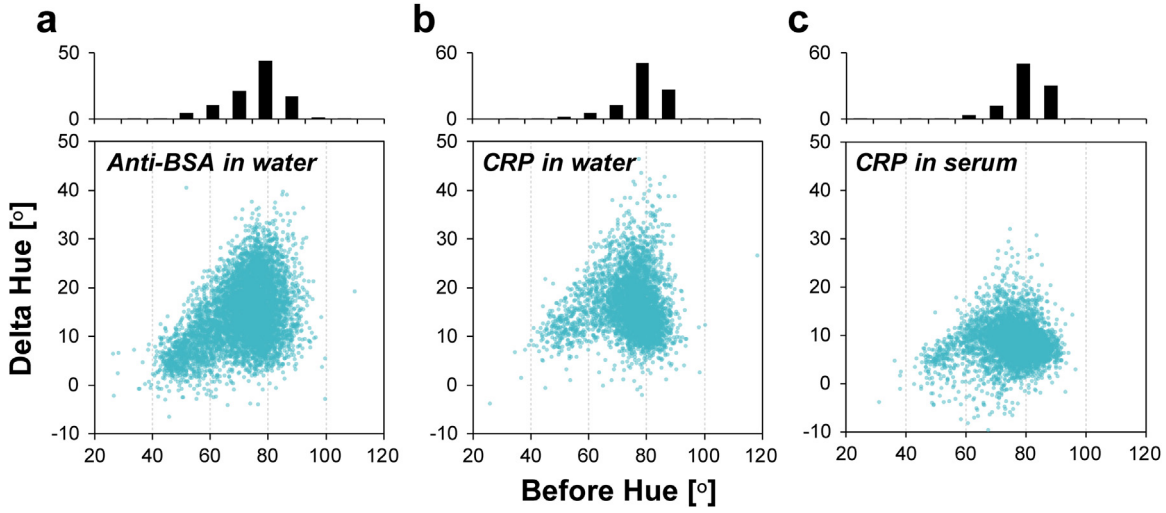

Fig. 5. Scatter plots of delta hue versus before-hue at equivalent concentrations. Each point in the scatter plot represents a single nanoparticle from the swarm. **(a)** anti-BSA in DI water at 100 nM; **(b)** CRP in DI water at 10 μg/ml (i.e., 87 nM); and **(c)** CRP spiked in serum at 10 μg/ml. The histogram above the scatter plots indicates the before-hue distribution for each group.

could indicate outliers with incomplete conjugation. Lower before-hue regions (< 60°) may be associated with non-specific binding to the nanoparticle surface during immobilization and potential particle aggregates. The range of the distribution along the y-axis (after-hue) for each before-hue region varies, which could be to the result of different numbers of analyte and detector probes bound to a single capture probe. The largest distribution of delta hue was typically around a before-hue near 80°, where the sensors were well-dispersed single nanoparticles fully conjugated to allow for the maximum number of binding sites available. Sensors exhibiting higher before-hues may generate a reduced hue shift because of less binding sites available after incomplete conjugation. The maximum delta hue (~40°) is achieved when a capture nanoparticle has the maximum number of binding sites all saturated by detector probes. Therefore, the distribution of delta hue at the lower before-hue region (< 60°) is limited to a smaller range, as indicated by the slope in the scatter plot. When detection occurred in serum, the maximum delta hue on y-axis was significantly lower with a much tighter distribution compared to that in buffer solution (Fig. 5**b-c**), possibly due to matrix effects in serum where some of the target antigen interacts with matrix components in serum instead of forming target antigen-antibody pairs. This informative sensing capability allows the evaluation of the sensor status for quality control, provides useful information for troubleshooting, and potentially enables protein marker dependent optimization.

4.6. Reduced instrument complexity for point-of-care applications

To minimize variations due to random noise and the inconsistency of the devices, either multiple measurements from the same device (e.g., LSPR biosensors equipped with spectrometers) or multiple measurements from different locations or wells (e.g., ELISA, PCR) are performed. Such an approach to make multiple measurements is limited by the cost, time, reagent usage, and instrument complexity for each sensing device. On the contrary, our swarm sensing approach using single nanoparticle colorimetry treats well-dispersed single nanoparticles as individual sensors that each get a vote as part of a swarm of parallel reactions. In addition, signal collection using dark field imaging instead of spectral shift measurements with spectrometers provides easy access to the location information of each nanoparticle, i.e., the swarm sensor. The combination of these two elements led to a low-cost solution for the simultaneous detection of hundreds of single particle sensors in one field of view, and normalization to an initial condition to avoid systematic error, which significantly increased the confidence in a measured result.

5. Conclusions

In summary, we have demonstrated a nanoplasmonic biosensing platform based on massively parallel analyses of a swarm of single nanoparticle colorimetric sensors, which provides informative sensing by evaluating sensor status both before and after sensing. Compared with some of the recently published works, our swarm sensor was able to achieve competitive performance across the board with wide dynamic range, low limit of detection, and relatively short assay time using small sample volumes (Table S3). Our swarm sensing scheme provides an alternative to conventional ensemble-based LSPR detection approaches. Our current dark-field setup with palm-size color camera provides a much smaller footprint compared to a conventional spectrometer with imaging components, and more cost-effectiveness than fluorescence microscopy. We are working on replacing the condenser with a total internal reflection illumination system to scale down the imaging component to be implemented as a handheld point-of-care device (Cetin et al., 2014; Kim et al., 2014; Wang et al., 2017). Rapid readouts from thousands of single particle sensors combined with individual evaluation using delta hue renders higher tolerance for particle variations, device variations, and sample variability. With minimized interference from non-specific binding in the background, the successful detection of clinical cutoffs within a close range of concentrations was possible in complex biofluids without the need of blocking steps. In addition, the simplicity of the sensor chip and particle preparation in colloidal solution without the need of nanofabrication significantly lowered the assay cost and make it a promising candidate for point-of-care readers using consumer electronics to perform dark-field imaging and multiplexed sensing (Gao et al., 2017; Lee et al., 2010; Zhao et al., 2016). Furthermore, the methodology of swarm sensing is versatile. Its application is not limited to nanoplasmonic platforms, and could be adapted by other types of single entity based sensors (e.g. fluorescence (Wang et al., 2013), electrochemical (Mohan et al., 2011), and magnetic (Sinha et al., 2014) for robust detection with statistically improved accuracy and reproducibility, as long as high-throughput readout from a large pool of individual sensors can be conducted efficiently using either imaging or other parallelized analysis methods.

CRediT authorship contribution statement

Mengxing Ouyang: Conceptualization, Data curation, Formal analysis, Methodology, Writing - original draft. **Dino Di Carlo:** Conceptualization, Funding acquisition, Supervision, Writing - review & editing.

Acknowledgments

This project is supported by the NSF-Engineering Research Center for Precise Advanced Technologies and Health Systems for Underserved Populations (PATHS-UP) - Award Number 1648451 and the Steven and Alexandra Cohen Foundation. We acknowledge the use of instruments at the Electron Imaging Center for NanoMachines (EICN) at the California NanoSystems Institute (CNSI) at University of California, Los Angeles.

Declaration of interests

None.

Appendix A. Supporting information

Supplementary data associated with this article can be found in the online version at doi:10.1016/j.bios.2019.02.056.

References

Adukauskiene, D., Ciginskiene, A., Adukauskaite, A., Pentiokiniene, D., Slapikas, R., Ceponiene, I., 2016a. Clinical relevance of high sensitivity C-reactive protein in cardiology. Medicina-Lith. 52 (1), 1–10.
Adukauskiene, D., Ciginskiene, A., Adukauskaite, A., Pentiokiniene, D., Slapikas, R., Ceponiene, I., 2016b. Clinical relevance of high sensitivity C-reactive protein in cardiology. Medicina (Kaunas.) 52 (1), 1–10.
Ament, I., Prasad, J., Henkel, A., Schmachtel, S., Sonnichsen, C., 2012. Single unlabeled protein detection on individual plasmonic nanoparticles. Nano Lett. 12 (2), 1092–1095.
Anker, J.N., Hall, W.P., Lyandres, O., Shah, N.C., Zhao, J., Van Duyne, R.P., 2008. Biosensing with plasmonic nanosensors. Nat. Mater. 7 (6), 442–453.
Brolo, A.G., 2012. Plasmonics for future biosensors. Nat. Photonics 6 (11), 709–713.
Cetin, A.E., Coskun, A.F., Galarreta, B.C., Huang, M., Herman, D., Ozcan, A., Altug, H., 2014. Handheld high-throughput plasmonic biosensor using computational on-chip imaging. Light-Sci. Appl. 3.
Chen, P.Y., Chung, M.T., McHugh, W., Nidetz, R., Li, Y.W., Fu, J.P., Cornell, T.T., Shanley, T.P., Kurabayashi, K., 2015. Multiplex serum cytokine immunoassay using nanoplasmonic biosensor microarrays. ACS Nano 9 (4), 4173–4181.
Chen, S., Svedendahl, M., Van Duyne, R.P., Kall, M., 2011. Plasmon-enhanced colorimetric ELISA with single molecule sensitivity. Nano Lett. 11 (4), 1826–1830.
Cheng, X.D., Dai, D.G., Yuan, Z.Q., Peng, L., He, Y., Yeung, E.S., 2014. Color difference amplification between gold nanoparticles in colorimetric analysis with actively controlled multiband illumination. Anal. Chem. 86 (15), 7584–7592.
Chiu, M.L., Lawi, W., Snyder, S.T., Wong, P.K., Liao, J.C., Gau, V., 2010. Matrix effects-a challenge toward automation of molecular analysis. Jala-J. Lab Autom. 15 (3), 233–242.
Csaki, A., Stranik, O., Fritzsche, W., 2018. Localized surface plasmon resonance based biosensing. Expert Rev. Mol. Diagn. 18 (3), 279–296.
Gao, Z., Ye, H., Tang, D., Tao, J., Habibi, S., Minerick, A., Tang, D., Xia, X., 2017. Platinum-decorated gold nanoparticles with dual functionalities for ultrasensitive colorimetric in vitro diagnostics. Nano Lett. 17 (9), 5572–5579.
Hall, W.P., Ngatia, S.N., Van Duyne, R.P., 2011. LSPR biosensor signal enhancement using nanoparticle-antibody conjugates. J. Phys. Chem. C 115 (5), 1410–1414.
Hao, J.R., Xiong, B., Chen, X.D., He, Y., Yeung, E.S., 2014. High-throughput sulfide sensing with colorimetric analysis of single Au-Ag core-shell nanoparticles. Anal. Chem. 86 (10), 4663–4667.
Hill, R.T., 2015. Plasmonic biosensors. Wiley Interdiscip. Rev. Nanomed. Nanobiotechnol. 7 (2), 152–168.
Im, H., Shao, H., Park, Y.I., Peterson, V.M., Castro, C.M., Weissleder, R., Lee, H., 2014. Label-free detection and molecular profiling of exosomes with a nano-plasmonic sensor. Nat. Biotechnol. 32 (5), 490–495.
Inci, F., Filippini, C., Baday, M., Ozen, M.O., Calamak, S., Durmus, N.G., Wang, S., Hanhauser, E., Hobbs, K.S., Juillard, F., Kuang, P.P., Vetter, M.L., Carocci, M., Yamamoto, H.S., Takagi, Y., Yildiz, U.H., Akin, D., Wesemann, D.R., Singhal, A., Yang, P.L., Nibert, M.L., Fichorova, R.N., Lau, D.T., Henrich, T.J., Kaye, K.M., Schachter, S.C., Kuritzkes, D.R., Steinmetz, L.M., Gambhir, S.S., Davis, R.W., Demirci, U., 2015. Multitarget, quantitative nanoplasmonic electrical field-enhanced resonating device (NE2RD) for diagnostics. Proc. Natl. Acad. Sci. USA 112 (32), E4354–E4363.
Jing, C., Gu, Z., Ying, Y.L., Li, D.W., Zhang, L., Long, Y.T., 2012. Chrominance to dimension: a real-time method for measuring the size of single gold nanoparticles. Anal. Chem. 84 (10), 4284–4291.
Johnsson, L., Baxter, G.A., Crooks, S.R.H., Brandon, D.L., Elliott, C.T., 2002. Reduction of sample matrix effects – the analysis of benzimidazole residues in serum by immunobiosensor. Food Agr. Immunol. 14 (3), 209–216.
Kim, B.N., Diaz, J.A., Hong, S.G., Lee, S.H., Lee, L.P., 2014. Dark-field smartphone microscope with nanoscale resolution for molecular diagnostics. In: Proceedings of the 18th International Conference on Miniaturized Systems for Chemistry and Life Sciences.
Landry, J.P., Ke, Y., Yu, G.L., Zhu, X.D., 2015. Measuring affinity constants of 1450 monoclonal antibodies to peptide targets with a microarray-based label-free assay platform. J. Immunol. Methods 417, 86–96.
Lee, H., Kim, J., Kim, H., Kim, J., Kwon, S., 2010. Colour-barcoded magnetic microparticles for multiplexed bioassays. Nat. Mater. 9 (9), 745–749.
Liang, K., Liu, F., Fan, J., Sun, D.L., Liu, C., Lyon, C.J., Bernard, D.W., Li, Y., Yokoi, K., Katz, M.H., Koay, E.J., Zhao, Z., Hu, Y., 2017. Nanoplasmonic quantification of tumour-derived extracellular vesicles in plasma microsamples for diagnosis and treatment monitoring. Nat. Biomed. Eng. 1 (4).
Lopez, G.A., Estevez, M.C., Soler, M., Lechuga, L.M., 2017. Recent advances in nanoplasmonic biosensors: applications and lab-on-a-chip integration. Nanophotonics-Berl. 6 (1), 123–136.
Mayer, K.M., Hao, F., Lee, S., Nordlander, P., Hafner, J.H., 2010. A single molecule immunoassay by localized surface plasmon resonance. Nanotechnology 21 (25).
McFarland, A.D., Van Duyne, R.P., 2003. Single silver nanoparticles as real-time optical sensors with zeptomole sensitivity. Nano Lett. 3 (8), 1057–1062.
Mohan, R., Mach, K.E., Bercovici, M., Pan, Y., Dhulipala, L., Wong, P.K., Liao, J.C., 2011. Clinical validation of integrated nucleic acid and protein detection on an electrochemical biosensor array for urinary tract infection diagnosis. PLoS One 6 (10), e26846.
Nguyen, A.H., Sim, S.J., 2015. Nanoplasmonic biosensor: detection and amplification of dual bio-signatures of circulating tumor DNA. Biosens. Bioelectron. 67, 443–449.
Pearson, T.A., Mensah, G.A., Alexander, R.W., Anderson, J.L., Cannon 3rd, R.O., Criqui, M., Fadl, Y.Y., Fortmann, S.P., Hong, Y., Myers, G.L., Rifai, N., Smith Jr., S.C., Taubert, K., Tracy, R.P., Vinicor, F., Centers for Disease, C., Prevention, American Heart, A.,, 2003. Markers of inflammation and cardiovascular disease: application to clinical and public health practice: a statement for healthcare professionals from the Centers for Disease Control and Prevention and the American Heart Association. Circulation 107 (3), 499–511.
Raschke, G., Kowarik, S., Franzl, T., Sonnichsen, C., Klar, T.A., Feldmann, J., Nichtl, A., Kurzinger, K., 2003. Biomolecular recognition based on single gold nanoparticle light scattering. Nano Lett. 3 (7), 935–938.
Rissin, D.M., Kan, C.W., Campbell, T.G., Howes, S.C., Fournier, D.R., Song, L., Piech, T., Patel, P.P., Chang, L., Rivnak, A.J., Ferrell, E.P., Randall, J.D., Provuncher, G.K., Walt, D.R., Duffy, D.C., 2010. Single-molecule enzyme-linked immunosorbent assay detects serum proteins at subfemtomolar concentrations. Nat. Biotechnol. 28 (6), 595–599.
Sinha, B., Ramulu, T.S., Kim, K.W., Venu, R., Lee, J.J., Kim, C.G., 2014. Planar Hall magnetoresistive aptasensor for thrombin detection. Biosens. Bioelectron. 59, 140–144.
Situ, C., Wylie, A.R.G., Douglas, A., Elliott, C.T., 2008. Reduction of severe bovine serum associated matrix effects on carboxymethylated dextran coated biosensor surfaces. Talanta 76 (4), 832–836.
Sonntag, M.D., Klingsporn, J.M., Zrimsek, A.B., Sharma, B., Ruvuna, L.K., Van Duyne, R.P., 2014. Molecular plasmonics for nanoscale spectroscopy. Chem. Soc. Rev. 43 (4), 1230–1247.
Spackova, B., Wrobel, P., Bockova, M., Homola, J., 2016. Optical biosensors based on plasmonic nanostructures: a review. Proc. IEEE 104 (12), 2380–2408.
Spadavecchia, J., Burras, A., Lyskawa, J., Woisel, P., Laure, W., Pradier, C.M., Boukherroub, R., Szunerits, S., 2013. Approach for plasmonic based DNA sensing: amplification of the wavelength shift and simultaneous detection of the plasmon modes of gold nanostructures. Anal. Chem. 85 (6), 3288–3296.
Springate, S.D., 2012. The effect of sample size and bias on the reliability of estimates of error: a comparative study of Dahlberg's formula. Eur. J. Orthod. 34 (2), 158–163.
Thevenaz, P., Ruttimann, U.E., Unser, M., 1998. A pyramid approach to subpixel registration based on intensity. IEEE Trans. Image Process 7 (1), 27–41.
Tokel, O., Inci, F., Demirci, U., 2014. Advances in plasmonic technologies for point of care applications. Chem. Rev. 114 (11), 5728–5752.
Ungureanu, F., Wasserberg, D., Yang, N., Verdoold, R., Kooyman, R.P.H., 2010. Immunosensing by colorimetric darkfield microscopy of individual gold nanoparticle-conjugates. Sens. Actuators B-Chem. 150 (2), 529–536.
Vashist, S.K., Luppa, P.B., Yeo, L.Y., Ozcan, A., Luong, J.H.T., 2015. Emerging technologies for next-generation point-of-care testing. Trends Biotechnol. 33 (11), 692–705.
Verdoold, R., Gill, R., Ungureanu, F., Molenaar, R., Kooyman, R.P.N., 2011. Femtomolar DNA detection by parallel colorimetric darkfield microscopy of functionalized gold nanoparticles. Biosens. Bioelectron. 27 (1), 77–81.
Wang, T.Y., Zhang, M., Dreher, D.D., Zeng, Y., 2013. Ultrasensitive microfluidic solid-phase ELISA using an actuatable microwell-patterned PDMS chip. Lab Chip 13 (21), 4190–4197.
Wang, X., Chang, T.W., Lin, G., Gartia, M.R., Liu, G.L., 2017. Self-referenced smartphone-based nanoplasmonic imaging platform for colorimetric biochemical sensing. Anal. Chem. 89 (1), 611–615.
Zhao, Z., Yang, Y., Zeng, Y., He, M., 2016. A microfluidic ExoSearch chip for multiplexed exosome detection towards blood-based ovarian cancer diagnosis. Lab Chip 16 (3), 489–496.
Zijlstra, P., Paulo, P.M.R., Orrit, M., 2012. Optical detection of single non-absorbing molecules using the surface plasmon resonance of a gold nanorod. Nat. Nanotechnol. 7 (6), 379–382.